Room-Temperature Measurement of Electrostatically Coupled, Dopant-Atom Double Quantum Dots in Point-Contact Transistors

Faris Abualnaja,[1] Chen Wang,[1,†] Vlad-Petru Veigang-Radulescu,[1,‡] Jonathan Griffiths,[2] Aleksey Andreev,[3] Mervyn Jones,[1] and Zahid Durrani[1,*]

[1] *Department of Electrical and Electronic Engineering, Imperial College London, South Kensington, London SW7 2AZ, United Kingdom*

[2] *Semiconductor Physics Group, Cavendish Laboratory, JJ Thomson Avenue, Cambridge CB3 0HE, United Kingdom*

[3] *A-Modelling Solutions Ltd., Forster Road, Guildford GU2 9AE, Surrey, United Kingdom*

(Received 11 July 2019; revised manuscript received 4 November 2019; published 23 December 2019)

The reduction of nanoelectronic devices to sub-10 nm sizes raises the prospect of electronics at the atomic scale, while also facilitating studies on nanoscale device physics. Single-atom transistors, where the current-switching element is formed by one atom and the information packet size is reduced to one electron, can create electronic switches scaled to their ultimate physical limits. Hitherto, single-atom transistor operation has been limited to low temperatures due to shallow quantum wells, which inhibit room-temperature nanoelectronic applications. Furthermore, the interaction between multiple single-atom elements at room temperature has yet to be demonstrated. Here, we show that quantum interactions between P dopants in $Si/SiO_2/Si$ single-atom transistors lead to room-temperature double quantum dot behavior. Hexagonal regions of charge stability and gate-controlled tunnel coupling between P atoms are observed at room temperature. Image processing is used to help reduce observer bias in data analysis. Single-electron device simulation is used to investigate evolution of the charge-stability region with varying capacitance and resistance. In combination with extracted tunnel capacitances and resistances, this allows experimental trends to be reproduced and provides information on the dopant-atom arrangement.

DOI: 10.1103/PhysRevApplied.12.064050

I. INTRODUCTION

Single-atom transistors [1–4], where the current-switching element is formed by one or a few atoms, extend the size scaling of electronic devices to their ultimate limit, at the atomic scale. Here, the switching element is small enough to behave inherently as a quantum dot (QD), which implies that the size scaling is also accompanied by a scaling of each information bit, to a minimal level of one electron per bit [5–7]. Device operation is inherently quantum mechanical, dominated by resonant tunneling and single-electron charging effects, and determined by the formation of discrete quantized energy states [8]. Hence, these devices raise the possibility of a fully quantum atomic-scale ultralow-power nanoelectronics memory and logic technology.

At present, most single-atom transistors use donor [3,4,9–16] and acceptor [1,2] substitutional impurity atoms within the Si channel of a field-effect transistor or single atoms deposited on atomically flat surfaces by scanning probe methods [4]. In these devices, electronic states associated with individual dopant-atom QDs [1,3,9,10] and with electrostatically coupled double QDs within a dopant-atom array [14–16] are measured and interactions between dopant-atom arrays formed by single-ion implantation methods [11] are characterized. However, such approaches rely on shallow, about 10–50 meV in depth, potential wells [3], which are insufficient to confine electrons at room temperature (RT). Device operation is thus limited to cryogenic temperatures only. While this is not a restriction for spectroscopic investigations of atomic states using electron tunneling [4], or for the definition of spin qubits using phosphorous (P) dopant atoms in silicon [17,18], the lack of RT operation prevents wider more general nanoelectronic logic, memory, or sensor applications.

Confining dopant atoms using tunnel barriers with heights that are considerably greater than those of the thermal fluctuations, $k_BT = 25$ meV at RT = 290 K, can enable the formation of RT single-atom transistors [19].

*z.durrani@imperial.ac.uk

†Present address: Department of Physics, Lancaster University, Bailrigg, Lancaster LA1 4YB, United Kingdom

‡Present address: Department of Engineering, University of Cambridge, 9 JJ Thomson Ave, Cambridge CB3 0FF, United Kingdom

 © 2019 American Physical Society

Dopant atoms within a wide-band-gap semiconductor or insulator can form deep-level states, where the quantum well depth may increase to about 1 eV or even larger [19,20]. However, such an atomic structure may be strongly isolated, reducing tunnel coupling [8,21] to source and drain electron reservoirs and other QDs, and limiting electrostatic control of energy states, thereby preventing QD transistor operation. Ideally, an atomic-scale nanoelectronic circuit using multiple single-atom transistor elements would require control over both tunnel coupling and the device energy states. Recently, we measured RT "Coulomb diamond" single-electron charging characteristics, as a function of a single gate voltage, in a P dopant-atom QD transistor, where the P atom was embedded within a $Si/SiO_2/Si$ tunnel junction [13,19]. In this structure, it is possible to observe both resonant tunneling and Coulomb diamond single-electron charging effects through an atomic-scale P QD placed between large source and drain regions and switching of the tunnel current by an electrostatically coupled gate. However, the existence of tunnel coupling and electrostatic interactions between individual RT atomic QD elements remains unclear.

Here, we demonstrate that electrostatically coupled double quantum dot (DQD) [21] operation at RT is possible using P dopant-atom dual-gate $Si/SiO_2/Si$ point-contact transistors. An array of P atom QDs embedded in a SiO_2 tunnel junction forms, which enables RT confinement of the associated atomic states. The RT dual-gate charge-stability characteristics (drain-source current I_{ds} vs gate voltages V_{gs1}, V_{gs2}) of these devices show hexagonal regions of charge stability [21] and gate-controlled tunnel coupling between P atoms, forming a complex pattern associated with randomness in the P array. Image-processing methods are used to automate the extraction of current peaks and hexagonal regions in the data; the latter form signatures of underlying electrostatically coupled DQDs. This use of image processing reduces the likelihood of observer bias in the analysis. Multiple hexagons are identified, which allow extraction of the corresponding tunnel capacitor network and variations in the effective capacitances and tunnel resistances as a function of gate voltages. Finally, single-electron transport simulation is used to investigate evolution of the hexagonal regions with varying capacitance and resistance, reproducing qualitatively patterns in experimental data. In combination with extracted capacitance and resistance values from the experimental data, this allows identification of specific DQD complexes within the dopant-atom array.

II. FABRICATION

The point-contact fabrication sequence is summarized in Fig. 1. Devices are fabricated using a silicon-on-insulator (SOI) wafer with an ultrathin 12 ± 1 nm heavily doped *n*-type Si top layer, with P at about 10^{20} cm^{-3} concentration [Fig. 1(a)]. A thin bilayer of PMMA resist is patterned by electron-beam lithography to form a lift-off pattern for aluminum deposition [Fig. 1(b)], which is subsequently used as a mask to pattern the underlying silicon by RIE [Fig. 1(c)]. This leaves embryonic source and drain contact regions still linked [Fig. 1(d)]. A geometric oxidation process [7,13,19] then both separates these contact regions by forming a SiO_2 tunnel junction at the point contact and leaves an array of isolated dopant atoms within the SiO_2 tunnel junction [Fig. 1(e)]; this is shown in greater detail in Fig. 2(a). Both single and coupled quantum dots result from this process. A schematic diagram of the QD energy levels, embedded in the oxide between the source and drain, is shown in Fig. 1(f). Further details on the fabrication process are given in Ref. [13].

A schematic diagram of the device, highlighting the distribution of P atoms, is shown in Fig. 2(a), accompanied by postoxidation scanning electron micrographs in Fig. 2(b). The equivalent circuit is shown in Fig. 2(c). The heavy doping of the device enables high conductivity to be retained up to the tips of the source and drain regions [Fig. 2(a)]. Device oxidation is sufficient to fully convert the point-contact region into SiO_2, but not the source, the drain, or the two gates nearby, where Si regions remain in the patterned cores, away from the surface [Fig. 2(a)]. Dopant atoms in these Si regions act as donors and form Fermi seas [Bohr radii are shown schematically by circles in Fig. 2(a)]; however, those atoms trapped within the SiO_2 point contact form a random array of quasi-isolated QDs [red dots in Fig. 2(a)]. The QDs create sites for electron tunneling from the source to the drain. The circuit diagram in Fig. 2(c) represents the general form of the QD array, where QDs in series or parallel configurations may interact with each other electrostatically or via tunnel coupling. In particular, we concentrate on DQD complexes (solid lines) because these can be identified electrically via their associated signature hexagonal charge-stability regions [21] in a plot of I_{ds} versus V_{gs1} and V_{gs2}. Here, T_M, T_L, and T_R are the mutual, left, and right tunnel barriers, respectively, for this DQD. Other QDs (dotted lines) may provide parallel current paths through the array. The various QDs also couple electrostatically to the two gate terminal voltages, e.g., through gate capacitances, $C_{gs1\text{–}4}$.

Scanning electron micrographs of two devices are shown in Fig. 2(b). The main high-resolution image shows a fully oxidized point contact of about 50 (width) $\times$ 30 (length) $\times$ 10 nm^3 (thickness). The inset shows a slightly larger device with a longer point contact. For the device in the main image, the original doped Si neck width is about 20 nm. This implies that dopants are randomly embedded in only a narrow 20-nm-wide section of SiO_2, giving a volume for the dopant array of about $20 \times 30 \times 10$ nm^3 (6000 nm^3). Potential routes to control dopant-position randomness include single-ion implantation from ion beams [11] or scanning probe methods [4].

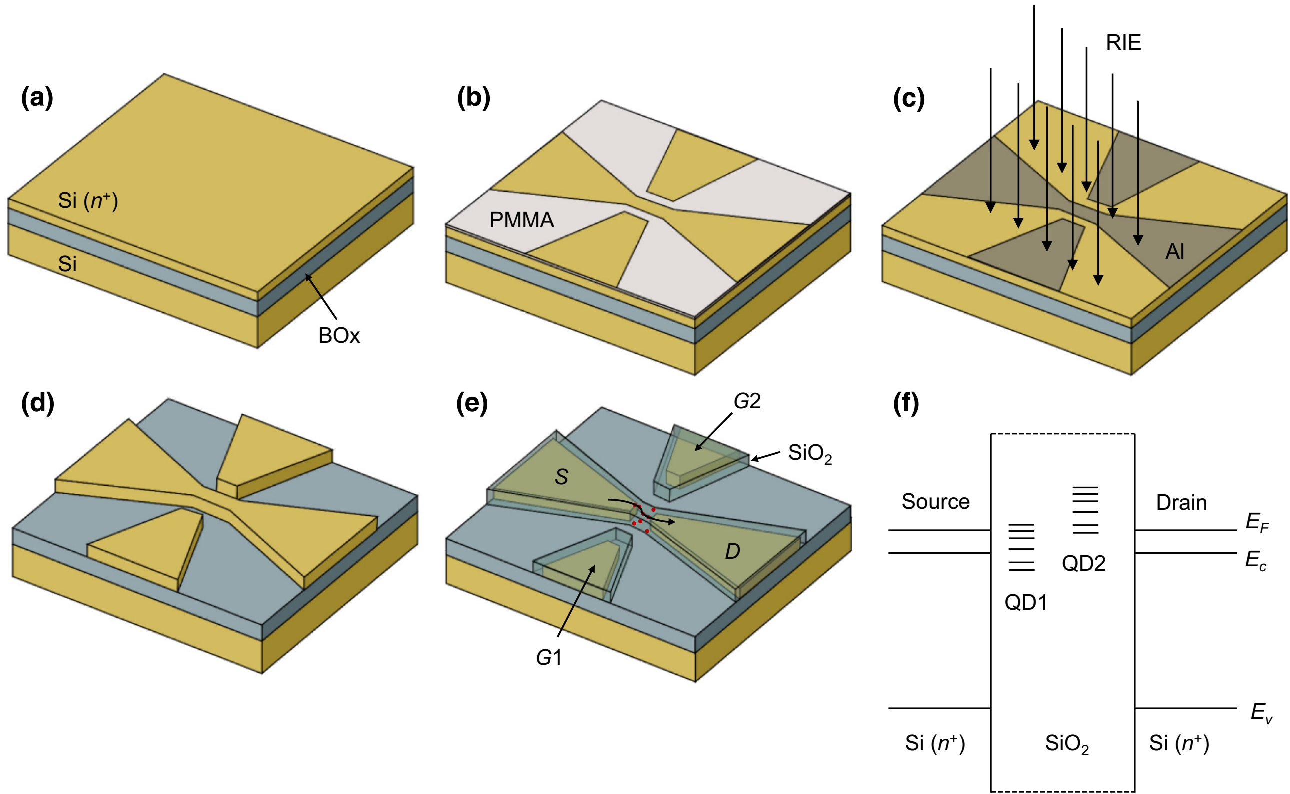

FIG. 1. Schematic representation of key process steps used to fabricate a point-contact device for RT DQDs. (a) Silicon-on-insulator wafer with buried oxide layer (BOx) and thin heavily n-doped top silicon ($\sim 10^{20}$ cm^{-3}). (b) Bilayer poly(methyl methacrylate) (PMMA) for aluminum lift-off after electron beam exposure and development. (c) Deposited Al is used as a mask for reactive-ion etching (RIE) of the top silicon layer. (d) Silicon structure on BOx after RIE. (e) Structure following geometric oxidation to form the source (S), drain (D), and gate ($G1$, $G2$) electrodes, together with QDs. (f) Schematic diagram of QD energy levels embedded in the oxide between the source and drain.

In our devices, with a doping density of about 10^{20}/cm^3, this implies an array of about 600 dopant atoms with an average separation of about 2 nm. The percolation path for conduction through this array is, however, likely to follow the shortest path between the source and drain regions, which implies that only a fraction of these atoms may participate in the device conduction. Atoms along or near the percolation path can then behave as QDs or interact in pairs to form DQD complexes, leading to current lines and peaks that define hexagonal regions in the charge-stability plot of I_{ds} versus V_{gs1} and V_{gs2}.

In our earlier work [13,19], single QD potential wells in similar devices were shown to be anharmonic, with diameters similar to that of the dopant separation. Variation in the dopant separation implies the following possibilities: (i) If dopant atoms in the SiO$_2$ barrier are very close, <2 nm, electronic states on these are delocalized, isolated QDs are not formed, and resistive conduction paths may form between source and drain regions, suppressing the observation of QD behavior. (ii) If dopant atoms are too widely dispersed, there can be no tunneling to the corresponding QDs and the device may form an open circuit. (iii) However, at an intermediate separation between dopant atoms, tunnel-isolated QDs can form and their electronic states measured electrically by tuning gate voltages. On rarer occasions, characteristics of double QDs can be studied, as reported here.

III. ELECTRICAL CHARACTERIZATION

Electrical characteristics at RT = 290 K for I_{ds} versus V_{gs1} and V_{gs2}, at a constant drain-source voltage (V_{ds}), are shown in Fig. 3. Data are shown for two different devices [Dev. A, Fig. 3(a), and Dev. B, Figs. 3(b)–3(d)]. Figure 3(c) is a subsection of data in Fig. 3(b) and shows the current peak slopes and layout in greater detail. The characteristics of Figs. 3(a)–3(c) are created by single-electron charging [5–8] of the QD array and correspond to the charge-stability diagram for these devices, in a similar manner to that of DQD devices [21]. The characteristics show current peaks and lines in I_{ds} clustered into polygonal honeycomblike patterns. Within a charge-stability diagram interpretation, crossing from one region to another corresponds to a change in the electron configuration

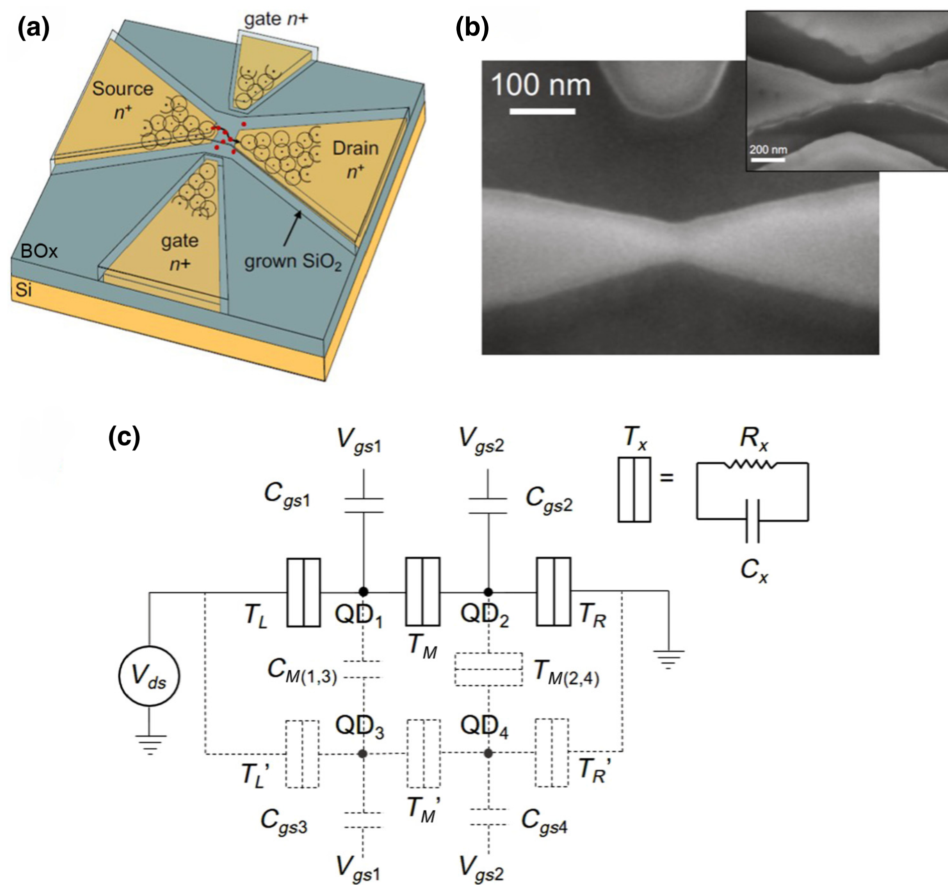

FIG. 2. Point-contact device for RT DQDs. (a) Schematic diagram of the silicon-on-insulator wafer. P dopant atoms with their Bohr radii (black dots and circles, respectively) are indicated within the top silicon region (colored gold). (b) SEM images of two devices. The main image shows a point-contact region in high resolution, where only one gate is visible; the inset image is a low-resolution image of a second device with a longer point contact. (c) The equivalent circuit diagram, illustrating arrays of QDs within the point-contact region. Each tunnel junction (T) corresponds to a resistor and capacitor in parallel, and the subscripts L, R, and M indicate the left, right, and mutual tunnel junctions, respectively.

of the QD array. In some cases [e.g., Fig. 3(a)], these patterns are hexagonal in nature and similar to those previously measured only in DQDs at cryogenic temperatures. In contrast to cryogenic DQD charge-stability plots, in our RT devices, current peaks are thermally broadened over a wider gate-voltage range. Measurements of the electrical characteristics are confined to RT. It has been shown previously [13] that, in these highly doped point-contact devices, with decreasing temperature, single-electron effects are masked by an increasingly significant potential barrier in series with the QD. This changes the shape and ultimately turns the device "off" and suppresses charge-stability regions in the measurement. The I_{ds}-V_{ds} characteristics for Dev. B, as V_{gs1} is stepped from 3.6 to 5.6 V, are shown in Fig. 3(d). A nonlinear I-V characteristic with a central "Coulomb blockade" region [5–7] is observed, with periodic modulation of the slope of the curves as single-current electron oscillations occur with V_{gs1}. Current modulation of this nature leads to the current peaks observed in the corresponding charge-stability plot.

The polygonal groups of current peaks in the electrical characteristics shown in Figs. 3(a)–3(c) appear very similar to the hexagonal charge-stability characteristics of multiple-donor-atom DQDs in Si FETs, as measured previously at cryogenic temperatures [15]. Unlike lithographically defined DQDs, the patterns in our characteristics are less regular. However, hexagonal "rings" can still be observed, e.g., the region marked α in Fig. 3(a). In each ring, the separation between two "triple points" [21] [e.g., the points at $(V_{gs1}, V_{gs2}) \approx (1.4, 1.6)$ and (1.5, 1.9)] is a measure of the strength of tunnel coupling between the two QDs in the DQD. Other areas, such as region β, show current peaks, where the location and shape suggest a partial hexagonal pattern. The current peaks also stretch to form zigzag lines, e.g., as V_{gs2} is varied at $V_{gs1} \approx 1.4$ V in Fig. 3(a) and along $V_{gs1} \approx 1.55$ V in Figs. 3(b) and 3(c). For the former case [Fig. 3(a)], a change in the length and current along sections with a positive slope (high current, red color) indicates a change in tunnel coupling with gate voltage. Finally, because the dopant-atom QDs embedded within the SiO_2 point contact are randomly located, this prevents the formation of an ideal periodic hexagonal honeycomb pattern across the entire charge-stability characteristic. However, hexagonal patterns are observed in multiple sections of the charge-stability characteristics [Figs. 3(a)–3(b)]. To analyze patterns within our data further, while avoiding any confirmation bias inherent with an inspection that is purely visual, image-processing methods are used to help extract potential polygonal regions, as described in Sec. IV.

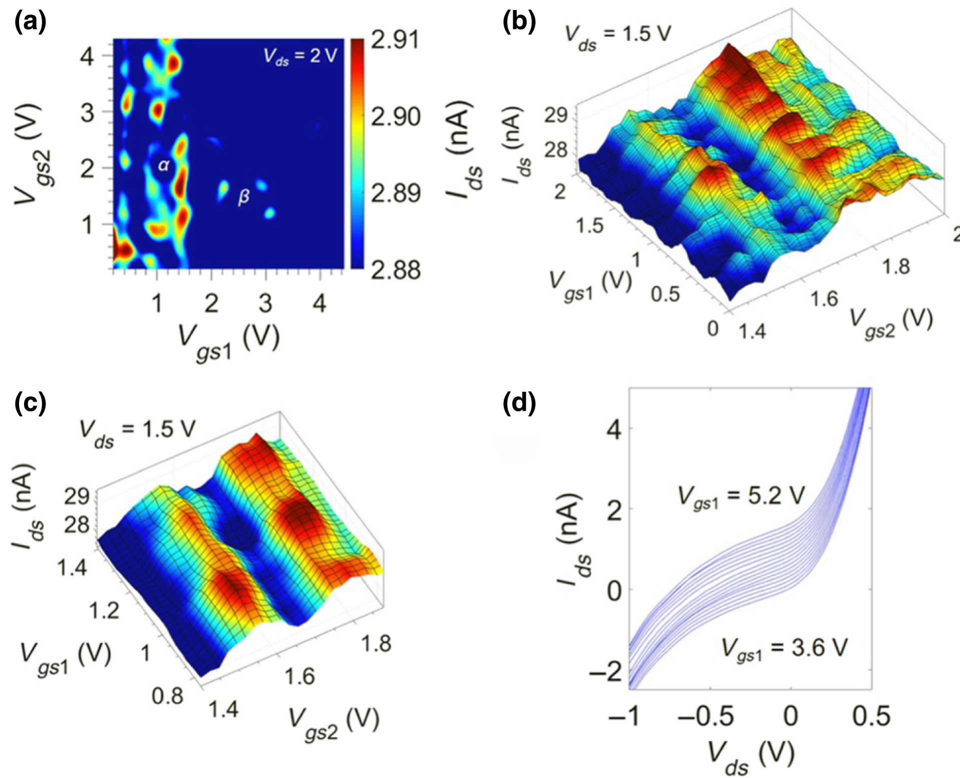

FIG. 3. Electrical characteristics at RT (290 K) for two separate point-contact DQD devices, Dev. A and Dev. B. (a) Drain-source current (I_{ds}) versus gate voltage (V_{gs1} and V_{gs2}) characteristics at constant drain-voltage (V_{ds}) for Dev. A, using a linear color scale. (b) I_{ds} versus $V_{gs1} = 0$–2 V and $V_{gs2} = 1.4$–2 V, at constant V_{ds}, for Dev. B. (c) I_{ds} versus $V_{gs1} = 0.8$–1.4 V and $V_{gs2} = 1.45$–1.9 V, at constant V_{ds}, for Dev. B. (d) I_{ds} versus V_{ds} characteristics for Dev. B, with values of $V_{gs1} = 3.6$–5.2 V, to illustrate the effects of V_{gs1} on the Coulomb blockade region. Each curve is at a constant V_{gs2} value.

IV. ANALYSIS

The random distribution of QDs within the dopant-atom array leads to a complex interaction circuit that links the QDs. Random variations occurring in the effective capacitances and resistances between the QDs [Fig. 2(c)] prevent the observation of a fully periodic honeycomb pattern, as seen in a single DQD system. However, the observation of only a limited number of hexagonal patterns in sections of the full charge-stability characteristics in Figs. 3(a)–3(c) implies the formation of only a few dominant DQD complexes at specific gate voltages. Across the entire charge-stability plot [e.g., Fig. 3(a), Dev. A], the number of current peaks, and associated polygonal or hexagonal patterns, is surprisingly small, given the random nature of the underlying dopant-atom array. This implies that only a limited number of dopant atoms contribute to the charge-stability plot. These atoms lie either along or near to a dominant percolation path passing through only a small fraction of the atoms in the dopant array and must couple strongly to the gate electrodes [22–24]. It may be expected that, as the minimum point-contact neck width increases, additional percolation paths begin to form, leading to a transition from electrical characteristics determined by a few QD complexes, to greater randomization in the characteristics, and ultimately to a bulk conduction mechanism.

Image processing is used to detect hexagonal pattern signatures of these DQD complexes. For this, The Otsu algorithm [25,26] is used to define a limited number (up to 5) of intensity thresholds in a histogram of the pixel intensity for a primary grayscale image of the characteristics. The segmentation of the primary continuous grayscale image by the Otsu algorithm reduces the influence of background fluctuations in intensity for the subsequent current-peak detection routine of the program, which is based on the Hough transformation [26–28]. These thresholds are then used to extract a secondary image with a reduced color scale, corresponding to these same thresholds. The secondary image allows the detection of prominent current maxima and enables polygonal patterns to be drawn. Figure 4 shows the results of this method applied to sections of data for Dev. A [Fig. 3(a)]. Potential hexagonal features may lie within the cropped regions: $V_{gs1} = 0.4$–1.8 V and $V_{gs2} = 1.2$–2.6 V, and $V_{gs1} = 1.8$–3.4 V and $V_{gs2} = 0.8$–2.0 V [Figs. 4(a) and 4(d), respectively]. For the later range of gate voltages, a potentially partial hexagonal feature is chosen for analysis. Secondary images created using the Otsu method are shown in Figs. 4(b) and 4(e), where the thresholds are 15.9%, 33.3%, 50.8%, 66.7%, and 85.7% of the maximum intensity for Fig. 4(b) and 9.5%, 22.2%, 33.3%, 42.9%, and 50.8% for Fig. 4(e). Furthermore, the algorithm allows the determination of both local current peaks and directional shifts in current magnitude within the original image. Following this, the algorithm looks for circular features within the extracted secondary image [Figs. 4(b) and 4(e)], corresponding to potential current peaks in the primary

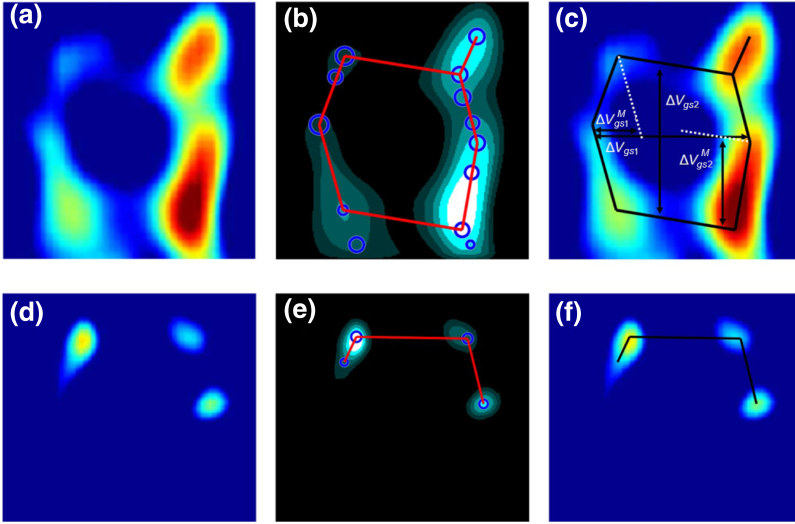

FIG. 4. Results of applying the Otsu image-processing algorithm to two specific parts of the electrical characteristics of Dev. A [Fig. 3(a)]. (a),(d) are two separate sections of the charge-stability plot shown in Fig. 3(a). (b),(e) are secondary threshold images, with local current peaks and directional shifts in current magnitude identified as blue circles. The centers of these circles are interconnected by applying theoretical restrictions to the slopes of the hexagon sides [16]. (c) The complete hexagon is superimposed onto the original color image (a), with hexagon dimensions labeled. (f) Potential hexagonal lines superimposed on the original color image (d).

image plot. Once the program has identified these features, the centers of the circles can be interconnected by lines to identify polygonal patterns [Figs. 4(b) and 4(e)]. For DQD interactions, the patterns should form hexagons, with restrictions on the slopes of the sides [21]. Only circle centers that do not violate these theoretical considerations are used. For example, for DQDs in series, two out of the six sides in the corresponding hexagonal pattern require positive slopes [top-left and bottom-right hexagon sides, e.g., see Figs. 4(b) and 4(e)], while the remaining four require negative slopes [21]. Further details of the operation of the image-processing method applied to these data are given in the Supplemental Material [29].

Following identification of hexagon patterns in the secondary threshold image, these may be superimposed on the original data image [Figs. 4(c) and 4(f)]. In Figs. 4(d)–4(f), a complete hexagon pattern is not detected, as the program only detects three sides and two corners of a partial pattern. However, the size of a detected hexagonal region may be used to extract effective capacitances and the circuit configuration of the DQD. Figure 5 shows results for the image-processing method extended to the full stability diagram image of Fig. 3(a). Both the current peaks extracted in Fig. 4 and additional current peaks can be seen throughout the image. Double QD hexagonal features can be located in the image and trends in the data analyzed. Three complete extracted hexagons (2, 4, and 5) and two possible partial hexagons (1 and 3) are seen in Fig. 5. The small number of clear hexagons in the data implies the existence of only a few DQD complexes, which are stable with varying gate voltage. As we observe relatively few hexagonal and other polygonal patterns in the data, this supports our picture of percolation conduction through only a fraction of the dopant array. Any changes in the effective capacitance network of the DQD with varying gate voltage lead to asymmetry or suppression of the hexagonal shapes.

V. SIMULATION AND DISCUSSION

Effective capacitances, C_L, C_M, C_R, C_{gs1}, and C_{gs2}, [Fig. 2(c)], are extracted for the DQD underlying the hexagon of Fig. 4(c). C_M provides a measure of the mutual tunnel coupling between the two QDs. The gate capacitances [21] are extracted directly: $C_{gs1} = |e|/\Delta V_{gs1} = 0.25$ aF and $C_{gs2} = |e|/\Delta V_{gs2} = 0.21$ aF, where ΔV_{gs1} and ΔV_{gs2} are the average width and height, respectively, of the hexagon [Fig. 4(c)]. An averaged width and height are used ($\Delta V_{gs1} = 0.65$ V and $\Delta V_{gs2} = 0.75$ V) to address any irregularities in the hexagon due to changes in the effective gate capacitances as a function of gate voltages. The hexagon dimensions may be given by the theoretical relationships [21] $\Delta V_{gs1} \approx \Delta V_{gs1}^{M}[((C_R + C_{gs2})/C_M) + 1]$ and $\Delta V_{gs2} \approx \Delta V_{gs2}^{M}[((C_L + C_{gs1})/C_M) + 1]$, where ΔV_{gs1}^{M} and ΔV_{gs2}^{M} are the horizontal and vertical Coulomb peak separations, respectively, marked in

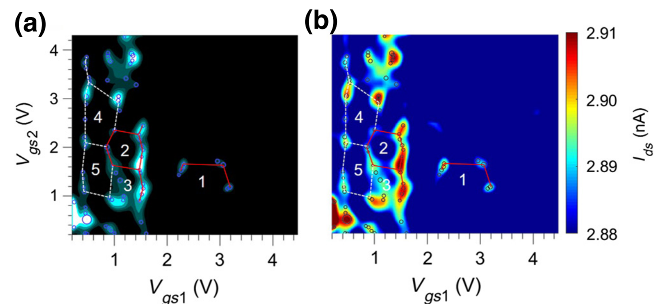

FIG. 5. The Otsu image-processing method applied to the full charge-stability plot of Fig. 3(a). (a) Secondary threshold image, where local current peaks and directional shifts in current magnitude are identified as blue circles. Interconnections between peaks are drawn by applying theoretical restrictions on the slopes of the hexagon's sides. (b) Superimposition of complete and partial hexagons on the original charge-stability plot.

Fig. 4(c). ΔV_{gs1}, ΔV_{gs2}, $\Delta V_{gs1}^{M_E}$, and $\Delta V_{gs2}^{M_E}$ can be measured from the hexagon dimensions, and C_{gs1} and C_{gs2} are extracted as shown earlier. For the remaining unknowns, C_L, C_M, and C_R, an assumption regarding the value of one of these is necessary. In our previous work [19], tunnel capacitance values in a single-gate point-contact device, with single QD characteristics, were found to be about 0.01 aF. Furthermore, data for Dev. A show moderate coupling between QDs because very strong coupling ($C_M \gg C_L, C_R$) leads to single-QD-like behavior (only diagonal lines would be observed), and weak coupling ($C_M \ll C_L, C_R$) leads to square patterns in the charge-stability plot [21]. The mutual capacitance is associated with the separation between the dopant-atom pair, which is, on average, about 2 nm for our doping concentration. A best fit is found for our data assuming $C_L = 0.05$ aF, giving $C_M \approx 0.20$ aF and $C_R \approx 0.25$ aF.

The charge-stability characteristics for a single hexagon (Fig. 5, hexagon 2) using these extracted constant effective capacitance values are evaluated with a single-electron tunneling simulation [30,31] in Fig. 6. A series DQD configuration is used, which best reflects the broadened peaks observed in our data. This simulator solves the master equation [6,31] for tunneling rates, and hence, determines the current for single-electron or QD circuits. The possibility of an arbitrary variation of the capacitances and tunneling resistances of the effective circuit as a function of the applied gate voltages is included in the simulation [30]. Figures 6(a)–6(c) show simulation results for the DQD corresponding to the hexagon of Fig. 4(c). A temperature dependence is simulated [Figs. 6(a)–6(c)] to verify that the thermally broadened and coalesced current peaks observed in our RT experimental data arise from well-separated peaks in our DQD simulation at low temperatures. The simulation image at 290 K [Fig. 6(c)] is annotated with the ideal simulated hexagon edges for clarity (black lines) and correctly reproduces the zigzag line observed in Dev. A as V_{gs2} varies with $V_{gs1} \approx 1.4$ V [Fig. 3(a)]. Any asymmetry in the experimentally measured hexagons in Dev. A can be attributed to interactions of DQD complexes with other nearby QDs and/or trapped charges. Finally, the current levels in Figs. 6(a)–6(c) are lower than those in experimental data for Dev. A, due to the low V_{ds} value used in the simulation ($V_{ds} = 0.01$ V). Parallel current paths would also increase the total device current in the experimental data.

Figures 6(d) and 6(e) show the effective gate capacitances [$C_{gs1(2)}$, marked by circles] versus the gate voltages ($V_{gs1(2)}$), which are extracted from the dimensions of hexagons 2–5 (Fig. 5). Values for C_{gs1} and C_{gs2} are estimated using averaged hexagon widths and heights. For partial hexagon 3 in Fig. 5, it is assumed that the remaining hexagon lines are symmetrical and parallel to those observed, and thus, allowing hexagon dimensions to be estimated. Capacitances for the partial hexagon 1 in Fig. 5 are not plotted because this requires greater extrapolation. $C_{gs1(2)}$ decrease with increasing $V_{gs1(2)}$, implying a trend of reducing effective gate capacitance as the associated gate voltage increases. The gate capacitance values [Fig. 6(d)] show some clustering into two groups, hexagons (2, 3) and (4, 5). This suggests either that each of these groups relate to a different underlying DQD complex or that C_{gs1} changes more strongly with V_{gs1} than that with V_{gs2}. For the former case, the two sets of hexagons, (2, 3) and (4, 5),

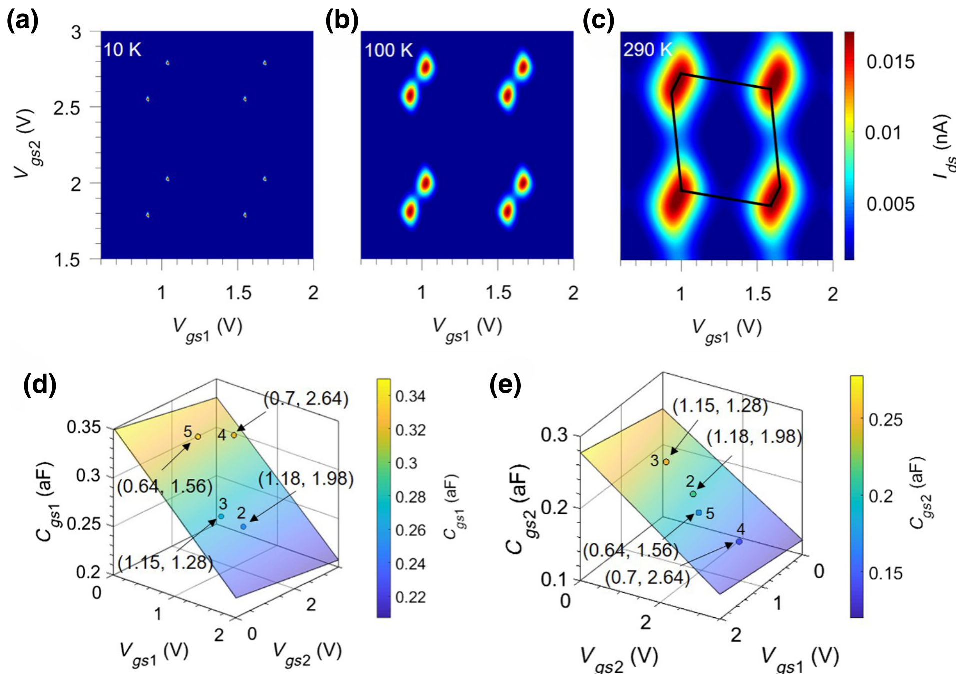

FIG. 6. Simulation results of extracted effective capacitances. (a)–(c) Temperature dependence (10, 100, and 290 K) of the DQD system. Here, $C_L = 0.05$ aF, $C_R = 0.25$ aF, $C_M = 0.20$ aF, $R_L = R_R = 10$ MΩ, and $R_M = 220$ MΩ. (d),(e) Effective gate capacitances [$C_{gs1(2)}$, marked by circles] versus the gate voltages ($V_{gs1(2)}$), extracted from hexagons 2–5 (Fig. 5). For each capacitance point, (V_{gs1}, V_{gs2}) values and the hexagon number, 2–4 (Fig. 5), are marked. Planes are fitted to these values to illustrate trends in the changes in $C_{gs1(2)}$.

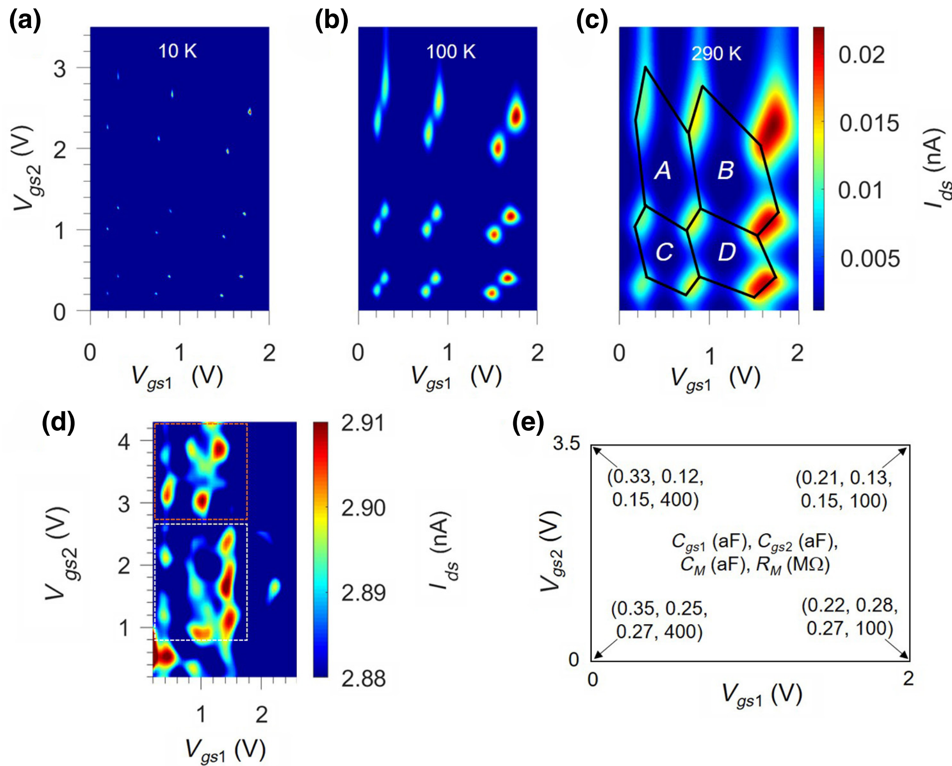

FIG. 7. Simulation results (a)–(c) for a single DQD complex, with linearly varying effective capacitances $C_{gs1(2)}$ and C_M and resistance R_M. These changes in capacitances and resistance are indicated in (e). (d) Subset of experimental data for comparison. (a)–(c) show simulations at 10, 100, and 290 K, respectively, over four hexagons, *A*–*D*. Results follow the experimental trends observed in (d) for the white dashed rectangle region. Trends in the orange dashed box are comparable to features found in Fig. 8(f).

and the isolated partial hexagon 1 would imply the existence of three DQD complexes. Figures 6(d) and 6(e) also show planes fitted to the extracted values of $C_{gs1(2)}$, tilted along both $V_{gs1(2)}$, to illustrate trends in the changes in $C_{gs1(2)}$.

The extracted linear dependences of the effective capacitances $C_{gs1(2)}$ with $V_{gs1(2)}$, represented by the planes in Figs. 6(d) and 6(e), are now used to simulate the changes in hexagon shape observed in experimental data of Fig. 5(b). Figures 7(a)–7(c) show results for four different hexagons (*A*–*D*) from a single DQD complex, at 10, 100, and 290 K. Figure 7(d) shows a subset of experimental data for comparison. Multiple DQD complexes are not simulated to avoid further complexity in the simulations. $C_{gs1(2)}$ are varied with $V_{gs1(2)}$ in a manner similar to the planes in Fig. 6(d) and 6(e). C_M is also varied linearly in a manner similar to that of $C_{gs1(2)}$, and the tunnel coupling resistance R_M is reduced with V_{gs1} to generate the increase in current observed in experimental data. Figure 7(e) shows the changes in C_{gs1}, C_{gs2}, C_M, and R_M, where the last two parameters correspond to changes in tunnel coupling. The variations in the hexagon heights [21] ($\Delta V_{gs2} = |e|/C_{gs2}$) and widths ($\Delta V_{gs1} = |e|/C_{gs1}$) [Figs. 7(a)–7(c)] follow trends seen in the experimental data [Fig. 7(d), white dashed rectangle region]. Here, a prominent increase in height occurs with V_{gs2} due to a significant change in C_{gs2}, and a relatively smaller increase in width occurs with V_{gs1}. The greater increase in hexagon height for lower values of V_{gs1} leads to a "twist" in the hexagon shape as V_{gs1} increases. Furthermore, the relatively strong reduction in C_{gs2} with V_{gs2} leads to a decoupling of V_{gs2} from the DQD and an elongation of the peak shape parallel to V_{gs2}. The peak separations [marked in Fig. 4(c)], determining the tunnel coupling, are given by [21] $\Delta V^M_{gs1} = \Delta V_{gs1}(C_M/C_2)$ and $\Delta V^M_{gs2} = \Delta V_{gs2}(C_M/C_1)$, where $C_{1(2)} = C_{L(R)} + C_{gs1(2)} + C_M$. Here, the most significant factor is the increase in $\Delta V_{gs1(2)}$, due to a reduction in $C_{gs1(2)}$, which leads to the increase in $\Delta V^M_{gs1(2)}$ seen in both experimental and simulation plots (Fig. 7).

With a view to explaining qualitatively changes in the hexagonal regions observed experimentally in Fig. 7(d), Fig. 8 simulates the evolution of an ideal periodic multiple-hexagon charge-stability diagram [Fig. 8(a)] with constant circuit parameters ($C_{gs1} = C_{gs2} = 0.25$ aF, $C_M = 0.2$ aF, $R_1 = R_2 = 10$ MΩ, $R_M = 2$ MΩ, $R = R_1 + R_2 + R_M = 22$ MΩ) as C_{gs1}, C_{gs2} [Figs. 8(b)–8(f)], C_M [Figs. 8(d)–8(f)], and R [Figs. 8(e) and 8(f)] are varied. Figures 8(a)–8(e) are simulated at 100 K to allow a clear observation of current peaks and changes in the hexagonal regions. Figure 8(f) simulates the variation of all parameters at 290 K, reproducing qualitatively many of the features in our experimental data [e.g., region with orange dashed rectangle, Fig. 7(d)]. One of the hexagonal regions is also marked (white lines) in all Figs. 8(a)–8(f) to trace changes in its size and shape as the underlying capacitances and resistances are varied.

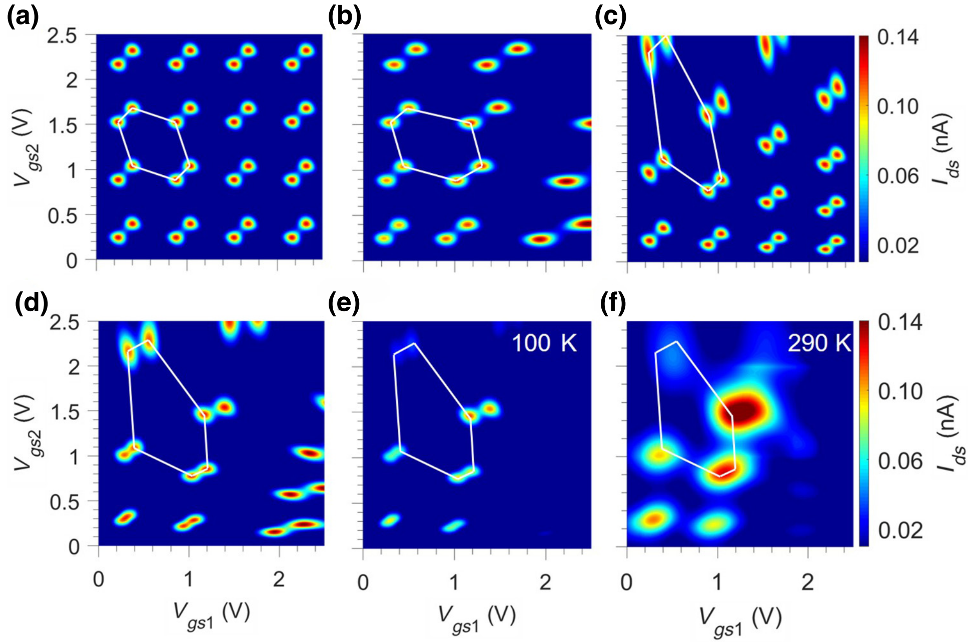

FIG. 8. (a)–(e) Evolution of DQD charge-stability diagram at 100 K, with a representative hexagon marked (white lines). (a) Ideal DQD charge-stability diagram, with $C_{gs1} = C_{gs2} = 0.25$ aF, $C_M = 0.20$ aF, $R = 22$ MΩ, $R_M = 2$ MΩ, $R_1 = 10$ MΩ, and $R_2 = 10$ MΩ. (b) Diagram (a), following linear reduction in C_{gs1} (0.3–0.175 aF) along V_{gs1} and V_{gs2} axes. At top-right corner, $C_{gs1} = 0.13$ aF (c) Diagram (a), following linear increase in C_{gs2} (0.25–0.42 aF) along V_{gs1} axis and linear decrease in C_{gs2} (0.25–0.17 aF) along V_{gs2} axis. C_{gs2} does not change along bottom-left to top-right diagonal. (d) Diagram (a) with the variation in C_{gs1} and C_{gs2} from (b),(c) combined. Additionally, C_M changes from 0.02 to 0.17 aF along V_{gs1} and V_{gs2} axes. At top-right corner, $C_M = 0.17$ aF. (e) Diagram (d), with additional piecewise linear variation in R, with values 22, 40, 220, and 820 MΩ at $V_{gs1} = 0$, 0.75, 1.5, and 2.5 V, respectively, and values of 22, 40, 130, and 160 MΩ at $V_{gs2} = 0$, 0.75, 1.5, and 2.5 V, respectively. (f) Diagram (e) simulated at 290 K, with a representative hexagon marked (white lines).

A comparison of Figs. 8(b) with 8(a) shows the effect of a linear reduction (0.3–0.175 aF) in C_{gs1} along V_{gs1} and V_{gs2} axes. With both V_{gs1} and V_{gs2}, this leads to an increase in width ΔV_{gs1} and triple-point separation ΔV^M_{gs1} of the hexagons, such that the peaks "fan out". In contrast, hexagon height ΔV_{gs2} does not change, as this depends on C_{gs2}. Figure 8(c) shows the corresponding trend for a combination of changes in C_{gs2}. Here, a linear increase (0.25–0.42 aF) in C_{gs2} with V_{gs1} and a linear decrease (0.25–0.17 aF) with V_{gs2} are used. An increase in hexagon height ΔV_{gs2} and triple-point separation ΔV^M_{gs2} is observed with V_{gs2} due to the reduction in C_{gs2} with V_{gs2}. In contrast, ΔV_{gs2} reduces with increasing V_{gs1} as C_{gs2} is increased. Figure 8(d) combines the effective capacitance changes in Figs. 8(b) and 8(c) (C_{gs1} reduces with V_{gs1} and V_{gs2}, and C_{gs2} increases with V_{gs1} and reduces with V_{gs2}). Furthermore, the effective coupling capacitance C_M is increased linearly (0.02–0.17 aF) with both V_{gs1} and V_{gs2}. This results in an increase in both $\Delta V_{gs1(2)}$ and $\Delta V^M_{gs1(2)}$ with $V_{gs1(2)}$, such that the peaks fan out prominently with increasing gate voltages, and the triple-point peaks tend to coalesce for lower C_M [lower $V_{gs1(2)}$] values. Figure 8(e) further adds an increase in total resistance R (22–820 MΩ) along V_{gs1} and 22–820 MΩ along V_{gs2}, to the simulation in (d), suppressing current peaks at larger gate voltages and switching-off the hexagonal pattern. Finally, Fig. 8(f) repeats the simulation of (e) at 290 K. Here, a thermally activated increase in current, combined with changes in capacitance and resistance, leads to a much more complex pattern, which qualitatively reproduces many features in our experimental data [e.g., the area within the orange dashed rectangle, Fig. 7(d)]. These features include broadening of current peaks, coalescing of triple points into larger irregular peaks, the formation of current "lines" along some hexagon sides, the observation of partial hexagons, and distortion of the shape of the hexagons.

Finally, we consider the possible cause of the observed changes in effective capacitances $C_{gs1(2)}$ and C_M and device resistance R with changing $V_{gs1(2)}$. This behavior forms the main driver for the change in the hexagon's shape. The simulations do not explicitly include the effect of size quantization in the QDs, which can change the peak separation with changes in electron number. The use of an effective capacitance allows a means to reflect on the influence of size quantization and the behavior of the quantized excited-state energy, E_k. Including excited states, the addition energy of an electron on a QD is given by

$E_n = E_c + E_k$, where $E_c = e^2/C$ is the charging energy of the QD with total capacitance C. Both E_c and E_k can vary with applied bias and electron number and, in this case, E_c can vary if the applied bias affects C, and E_k depends on the size and shape of the QD potential well. Our previous work [19] on single-donor QDs in SiO_2 demonstrated the formation of anharmonic potential wells in these systems. Variation in gate voltage can change the shape of these wells, leading to changes in the effective capacitances, tunnel resistances and energy states E_c and E_k. Furthermore, for a narrow and steep potential well, the energy-state separation, $\Delta E = E_{k+1} - E_k$, near the bottom of the well increases with k for the first few values of k, leading to an increase in Coulomb diamond widths with increasing gate voltage for a single QD. A similar effect in a DQD complex would increase the hexagon heights and widths, corresponding to a reduction in the effective gate capacitances, $C_{gs1(2)}$, in a manner similar to that in our model.

VI. SUMMARY

In conclusion, electrostatically coupled DQD operation at RT is possible using P dopant-atom dual-gate $Si/SiO_2/Si$ point-contact transistors. An array of P atom QDs embedded in a SiO_2 tunnel junction is formed to enable RT confinement of the associated atomic states. The RT dual-gate charge-stability characteristics show hexagonal regions of charge stability and gate-controlled tunnel coupling between P atoms, forming a complex pattern associated with randomness in the P array. Image-processing methods automate the identification of current peaks and hexagonal regions in data and reduce observer bias. The identified hexagons allow extraction of the corresponding tunnel capacitor network and demonstrate the dependence of the tunnel and gate coupling on the gate voltages. Single-electron simulation using the extracted capacitance and resistance values reproduce the patterns observed in experimental data, and thus, allow identification of specific DQD complexes within the dopant-atom array. The evolution of an ideal periodic hexagonal charge-stability diagram in the presence of varying capacitances, resistances, and temperature is traced, to reproduce qualitatively additional features and patterns in our experimental data.

The results of this paper further extend electron-transport models for impurities in insulators and illustrate the extent of thermal stability in dopant-atom QD interactions. Previously, the electrical properties of insulators, particularly gate oxide layers in field-effect transistors, have been investigated in depth, mainly for large-area samples, with an emphasis on capacitive measurements [22,32]. In contrast, microscopic conduction and tunneling mechanisms are comparatively neglected. Our data show that such processes may be understood in terms of the formation of impurity-atom QD arrays and percolation paths through these arrays. Even for a random array, at the local microscopic level, electrostatic interactions and single-electron charging of impurity atoms is significant at RT. Potential routes to controlling randomness include single-ion implantation from ion beams [11] or scanning probe methods [4]. Coupled dopant-atom QD behavior is therefore significant not only at cryogenic temperatures, but, given deep enough dopant-atom quantum wells, this behavior also determines the conduction properties, even at RT.

ACKNOWLEDGMENTS

The authors would like to acknowledge valuable discussions at Imperial College London with Dr. Dixi Liu, regarding device fabrication and measurement, and Prof. Richard Syms, regarding image-processing methods and analysis. F.A. would like to acknowledge financial support from the UK Engineering and Physical Sciences Research Council (EPSRC) Quantum System Engineering (QSE) Skills Training Hub.

[1] H. Sellier, G. P. Lansbergen, J. Caro, S. Rogge, N. Collaert, I. Ferain, M. Jurczak, and S. Biesemans, Transport Spectroscopy of a Single Dopant in a Gated Silicon Nanowire, Phys. Rev. Lett. **97**, 206805 (2006).

[2] L. E. Calvet, R. G. Wheeler, and M. A. Reed, Observation of the Linear Stark Effect in a Single Acceptor in Si, Phys. Rev. Lett. **98**, 096805 (2007).

[3] M. Pierre, R. Wacquez, X. Jehl, M. Sanquer, M. Vinet, and O. Cueto, Single-donor ionization energies in a nanoscale CMOS channel, Nat. Nanotechnol. **5**, 133 (2010).

[4] M. Fuechsle, J. A. Miwa, S. Mahapatra, H. Ryu, S. Lee, O. Warschkow, L. C. Hollenberg, G. Klimeck, and M. Y. Simmons, A single-atom transistor, Nat. Nanotechnol. **7**, 242 (2012).

[5] K. K. Likharev, Single-electron devices and their applications, Proc. IEEE **87**, 606 (1999).

[6] Z. A. K. Durrani, *Single-Electron Devices and Circuits in Silicon* (Imperial College Press, London, 2010).

[7] Y. Takahashi, Y. Ono, A. Fujiwara, and H. Inokawa, Silicon single-electron devices, J. Phys. Condens. Mater. **14**, R995 (2002).

[8] L. P. Kouwenhoven, C. M. Marcus, P. L. Mceuen, S. Tarucha, R. M. Westervelt, and N. S. Wingreen, Electron transport in quantum dots, Nato Adv. Sci. I E-App. **345**, 105 (1997).

[9] K. Y. Tan, K. W. Chan, M. Mottonen, A. Morello, C. Yang, J. V. Donkelaar, A. Alves, J. M. Pirkkalainen, D. N. Jamieson, R. G. Clark, and A. S. Dzurak, Transport spectroscopy of single phosphorus donors in a silicon nanoscale transistor, Nano Lett. **10**, 11 (2010)..

[10] D. Moraru, A. Udhiarto, M. Anwar, R. Nowak, R. Jablonski, E. Hamid, J. C. Tarido, T. Mizuno, and M. Tabe, Atom

devices based on single dopants in silicon nanostructures, Nanoscale Res. Lett. **6**, 479 (2011).

[11] E. Prati, M. Hori, F. Guagliardo, G. Ferrari, and T. Shinada, Anderson-Mott transition in arrays of a few dopant atoms in a silicon transistor, Nat. Nanotechnol. **7**, 443 (2012).

[12] V. V. Shorokhov, D. E. Presnov, S. V. Amitonov, Y. A. Pashkin, and V. A. Krupenin, Single-electron tunneling through an individual arsenic dopant in silicon, Nanoscale **9**, 613 (2017).

[13] Z. A. Durrani, M. E. Jones, C. Wang, D. Liu, and J. Griffiths, Excited states and quantum confinement in room temperature few nanometre scale silicon single electron transistors, Nanotechnology **28**, 125208 (2017).

[14] E. Prati, M. Belli, S. Cocco, G. Petretto, and M. Fanciulli, Adiabatic charge control in a single donor atom transistor, Appl. Phys. Lett. **98**, 053109 (2011).

[15] B. Roche, E. Dupont-Ferrier, B. Voisin, M. Cobian, X. Jehl, R. Wacquez, M. Vinet, Y. M. Niquet, and M. Sanquer, Detection of a Large Valley-Orbit Splitting in Silicon with Two-Donor Spectroscopy, Phys. Rev. Lett. **108**, 206812 (2012).

[16] B. Roche, R. P. Riwar, B. Voisin, E. Dupont-Ferrier, R. Wacquez, M. Vinet, M. Sanquer, J. Splettstoesser, and X. Jehl, A two-atom electron pump, Nat. Commun. **4**, 1581 (2013).

[17] J. J. Pla, K. Y. Tan, J. P. Dehollain, W. H. Lim, J. J. L. Morton, D. N. Jamieson, A. S. Dzurak, and A. Morello, A single-atom electron spin qubit in silicon, Nature **489**, 541 (2012).

[18] K. Saeedi, S. Simmons, J. Z. Salvail, P. Dluhy, H. Riemann, N. V. Abrosimov, P. Becker, H. J. Pohl, J. J. Morton, and M. L. Thewalt, Room-temperature quantum bit storage exceeding 39 minutes using ionized donors in silicon-28, Science **342**, 830 (2013).

[19] Z. Durrani, M. Jones, F. Abualnaja, C. Wang, M. Kaestner, S. Lenk, C. Lenk, I. W. Rangelow, and A. Andreev, Room-temperature single dopant atom quantum dot transistors in silicon, formed by field-emission scanning probe lithography, J. Appl. Phys. **124**, 144502 (2018).

[20] D. Han, D. West, X. B. Li, S. Y. Xie, H. B. Sun, and S. B. Zhang, Impurity doping in SiO_2: Formation energies and defect levels from first-principles calculations, Phys. Rev. B **82**, 155132 (2010).

[21] W. G. van der Wiel, S. De Franceschi, J. M. Elzerman, T. Fujisawa, S. Tarucha, and L. P. Kouwenhoven, Electron transport through double quantum dots, Rev. Mod. Phys. **75**, 1 (2003).

[22] B. I. Shklovskiĭ and A. L. ėfros, *Electronic Properties of Doped Semiconductors* (Springer-Verlag, Berlin, New York, 1984), Springer series in solid-state sciences, 45.

[23] M. A. Rafiq, Y. Tsuchiya, H. Mizuta, S. Oda, S. Uno, Z. A. K. Durrani, and W. I. Milne, Hopping conduction in size-controlled Si nanocrystals, J. Appl. Phys. **100**, 014303 (2006).

[24] M. A. H. Khalafalla, H. Mizuta, and Z. A. K. Durrani, Identifying single-electron charging islands in a two-dimensional network of nanocrystalline silicon grains using Coulomb oscillation fingerprints, Phys. Rev. B **74**, 035316 (2006).

[25] N. Otsu, Threshold selection method from gray-level histograms, IEEE Trans. Syst. Man Cybern. **9**, 62 (1979).

[26] M. Demirci, Matlab image-processing toolbox, Computer **27**, 106 (1994).

[27] R. O. Duda and P. E. Hart, Use of hough transformation to detect lines and curves in pictures, Commun Acm. **15**, 11 (1972).

[28] T. J. Atherton and D. J. Kerbyson, Size invariant circle detection, Image Vision Comput. **17**, 795 (1999).

[29] See the Supplemental Material at http://link.aps.org/supplemental/10.1103/PhysRevApplied.12.064050 for more details on the image-processing program used.

[30] A. Andreev, Modelling transport in Coulomb blockade regime using effective capacitance model (in preparation).

[31] M. Kirihara, K. Nakazato, and M. Wagner, Hybrid circuit simulator including a model for single electron tunneling devices, Jpn. J. Appl. Phys. **38**, 2028 (1999).

[32] S. S. Nekrashevich and V. A. Gritsenko, Electronic structure of silicon dioxide (a review), Phys. Solid State **56**, 207 (2014).